Supplementary Materials on
Enhancing Uncrewed Aerial Vehicle Techniques for Monitoring Greenhouse Gas Plumes at Point Sources

Horim Kim[a,b,1], Keun Taek Kim[a,1], Sangjae Jeong[c,*], Young Su Lee[d], Xin Zhao[a], Jae Young Kim[a,*]

[a]*Department of Civil and Environmental Engineering, Seoul National University, Seoul, Republic of Korea*
[b]*Institute of Construction and Environmental Engineering, Seoul National University, Seoul, Republic of Korea*
[c]*Department of Civil and Environmental Engineering, Hanbat National University, Daejeon, Republic of Korea*
[d]*Department of Energy and Environmental Engineering, Soonchunhyang University, Asan, Republic of Korea*

Table of Contents

*Corresponding authors at: Department of Civil and Environmental Engineering, Hanbat National University, Daejeon, Republic of Korea (Sangjae Jeong); Department of Civil and Environmental Engineering, Seoul National University, Seoul, Republic of Korea (Jae Young Kim)

Email addresses: sangjae.jeong@hanbat.ac.kr (Sangjae Jeong), jaeykim@snu.ac.kr (Jae Young Kim)

[1]These authors are equal contributors to this work and are designated as co-first authors.

Note S1. Scale difference between UAV and the incinerator stack during the flight operations

(a)

(b)

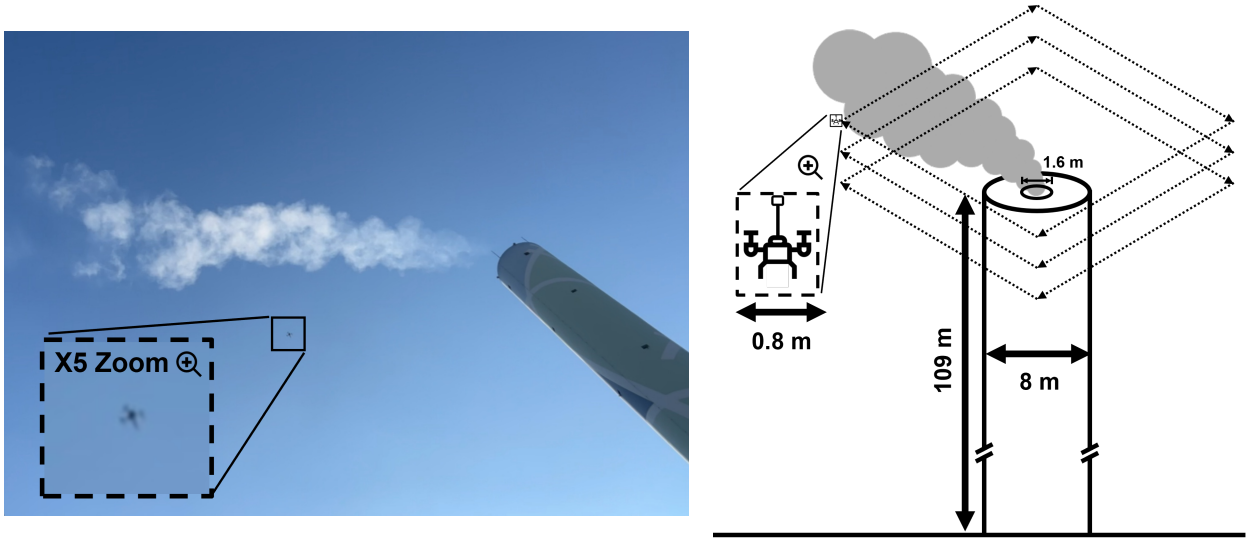

Figure S1: Scale difference between UAV and the incinerator stack during the flight operations. (a) A picture captured during a UAV flight operation near the incinerator stack. The inset shows a zoomed-in view of the UAV. (b) Schematic diagram illustrating the dimensions of the UAV and the incinerator stack.

Note S2. Detailed information on the measurement instrumentation

Note S2.1. UAV specification

The primary component of our monitoring system is the DJI Matrice 300 RTK (see Figure S2), manufactured by DJI Technology Inc. This quadcopter, weighing approximately 6 kg when equipped with two batteries, can carry a maximum payload of 2.7 kg. The drone's dimensions with the propeller arms unfolded are 810 × 670 × 430 mm (Length x Width x Height). Although the manufacturer specifies a maximum flight time of 55 minutes, our field experiment experience suggests that a practical maximum flight time is around 25 minutes with the sensor system payloads, considering operational safety. Typically, we concluded missions when the battery level fell to less than 30 % to ensure safety.

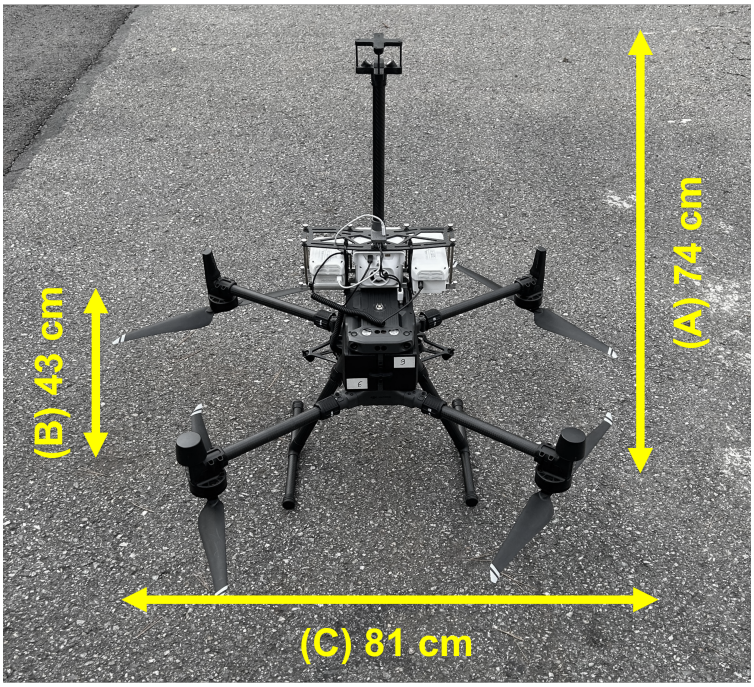

Figure S2: DJI Matrice 300 RTK equipped with onboard sensors for air quality monitoring. The height atop of the sensors (A) is 74 cm. The length of a UAV with arms unfolded (C) is 81 cm wide and the height of the main body (B) is 43 cm.

Note S2.2. Sensor Module

The onboard sensor system, custom-developed by Soarability Technology LLC (Shenzhen, China), comprises four sensor modules (see Figure S3), each also engineered by the developer. The entire sensor suite, along with its titanium-based mounting fixtures, adds approximately 2 kg to the UAV's payload. Detailed specifications for each sensor module are provided below:

1. A sonic anemometer is positioned 40 cm above the main body to measure wind speed and direction by minimizing hindrance from the propeller winds. The original sensor is a 3-D sonic

anemometer (Geotech Inc, Denver, USA, model TriSonica Mini), custom-developed algorithms by the manufacturer correct for the UAV's translational motion, attitude changes, and rotational motion, ensuring reliable wind data even during flight. The algorithm-calibrated anemometer provides two-dimensional horizontal wind data. The anemometer measures wind speeds from 0 to 50 $m\,s^{-1}$ with a resolution of 0.1 $m\,s^{-1}$, achieving accuracies of ± 0.1 $m\,s^{-1}$ for wind speeds up to 10 $m\,s^{-1}$, ± 1% for wind speeds between 11 and 30 $m\,s^{-1}$, and ± 2 % for the wind speed range of 31 to 50 $m\,s^{-1}$. Wind direction is measured within a 0 to 360 ° range, with a resolution and accuracy of 1.0 °.

2. Non-dispersive Infrared (NDIR) CO_2 sensor offers a measurement range of 0 to 2,000 ppm and has a detection limit of 1 ppm, with a theoretical resolution of 1 ppm. Laboratory tests conducted by the manufacturer have demonstrated that the sensor achieves the technical accuracy of ± 3 % of the full-scale reading for CO_2 measurements up to 4,000 ppm. The sensor responds in less than 3 seconds when operating at a standard flow rate of 500 ml/min. A brief warm-up period of 3 minutes is required from a cold start for optimal performance. The sensor functions within a temperature range of -20 to 50 $°C$ and can tolerate relative humidity levels up to 85%.

3. The main module, named *Sniffer4D V2*, is designed to support a variety of internally mounted modules for measuring both gaseous pollutants and particulate matter. It includes built-in LTE connectivity for real-time data transmission over global 4G, 3G, EDGE, and GPRS networks. Additionally, the system is equipped with a high-precision Global Navigation Satellite System (GNSS) ensuring accurate location tracking without the need for an external antenna.

   The Sniffer4D V2 module utilized in this study was customized to provide GPS coordinates (altitude, longitude, latitude), environmental parameters (temperature, humidity, pressure), and concentrations of gaseous pollutants (VOCs, CO, NO_2, O_3), alongside particulate matter ($PM_{1.0}$, $PM_{2.5}$, PM_{10}).

   The Particulate Matter Sensing Module delivers measurements of $PM_{1.0}$, $PM_{2.5}$, PM_{10} levels within a range of 0 to 1000 $\mu g\,m^{-3}$, achieving a resolution of 1 $\mu g\,m^{-3}$. Electro-chemical sensors are utilized for precise detection of each gaseous pollutant: the O_3 sensor identifies concentrations up to 11 ppm with a theoretical resolution below 1 ppb; the NO2 and CO sensors are capable of measuring up to 11 ppm, with theoretical resolutions of less than 1.1 ppb and 0.6 ppb, respectively. Additionally, the TVOC module, primarily targeting isobutylene, covers a range of 0 to 50 ppm with a theoretical resolution of 3.8 ppb.

   The module can also monitor environmental variables. Temperature sensor operated within a range of -40 to 80 °C, offering an accuracy of ± 0.1 to ± 0.4 °C. Humidity is measured from 0 to 100 % RH, with accuracy levels of ± 1.5 % to ± 2.5 % RH. The atmospheric pressure sensor delivers readings from 33 to 110 kPa, detailed to a resolution of 0.1 kPa and an accuracy of ± 1.0 kPa.

4. Tunable Diode Laser Absorption Spectroscopy (TDLAS) based CH_4 sensor operates on a closed-path TDLAS detection method with an output rate of 1 Hz. The sensor covers

a measurement range of 0 to 15,000 ppm and achieves a detection limit of 1 ppm and a theoretical resolution of 1 ppm.

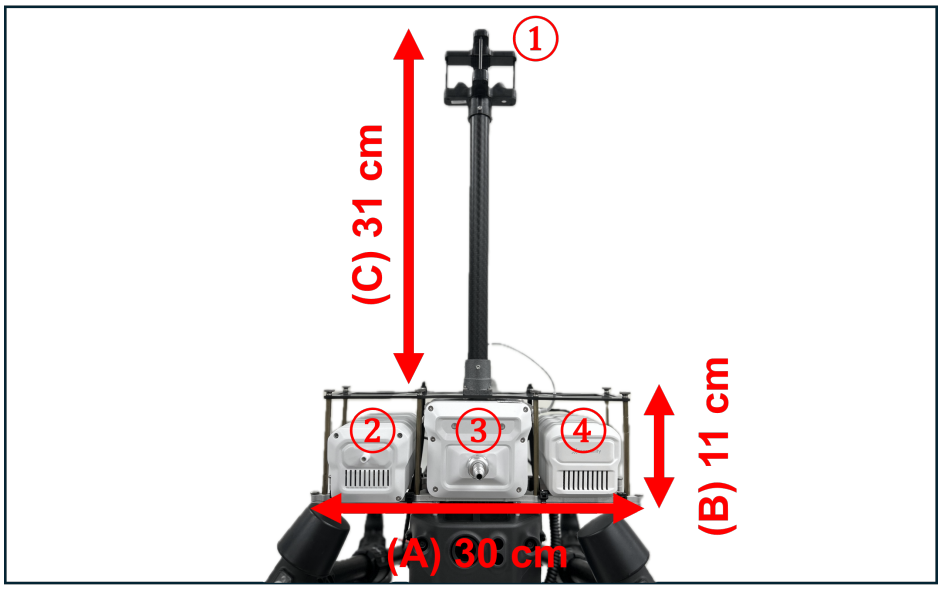

Figure S3: Detailed view of the UAV's onboard sensor configuration, showing ① the anemometer mounted on an aluminum 31 cm rod (C), the ② CO_2 sensor module, ③ the electro-chemical sensor module, and ④ the CH_4 sensor module, all securely attached to the UAV frame. The sensor array spans a width of 30 cm (A) and a height of 11 cm (B).

The sensor system is powered by the DJI Matrice 300's batteries. Data from the four sensor modules are compiled within the Sniffer4D V2 module, which records the data at a temporal resolution of one second. For real-time verification and sensor status monitoring during field experiments, the Sniffer4D Mapper software from Soarability is used. This tool allows for the real-time visualization of data via 2-dimension and 3-dimension concentration heat maps, facilitating the assessment of sensor functionality and identification of any operational issues during the flight mission. The Sniffer4D Mapper supports exporting the collected data into CSV format for data analysis.

Note S2.3. Ground Weather station

In this study, the Vantage Pro2 weather station (Davis Instruments, Hayward, CA, USA) was used to gather meteorological data. It measures wind direction within a 0° to 360° range, with a resolution of 1° and accuracy of ±3°. Wind speed capabilities range from 1 m s^{-1} to 80 m s^{-1}, with a resolution of 0.1 m s^{-1} and accuracy of ±3%. Humidity is measured from 1% to 100%, with a resolution of 1% and accuracy of ±5%. Temperature readings span from 0 °C to 60 °C, with a resolution of 0.1 °C and accuracy of ±0.3°C. Barometric pressure is recorded from 410 mmHg to 820 mmHg, with a resolution of 0.1 mmHg and an accuracy of ±0.8 mmHg. Solar radiation is captured from 0 W m^{-2} to 1800 W m^{-2}, with a resolution of 1 W m^{-2} and accuracy of ±5%.

Note S3. A strategy for selecting UAV takeoff and landing points

Identifying a suitable takeoff and landing point for the UAV flight mission is important when arriving at the site. Several considerations influenced this decision: the point needed to be close enough to the actual flight routes to minimize power consumption during UAV takeoff and landing, thereby maximizing available flight time for monitoring missions. Additionally, it was critical to select a location that was safely distanced from industrial activities and free from aerial obstacles, such as trees and street lamps, that could hinder UAV operations. The ideal takeoff point should offer clear visibility of the plume and facilitate unobstructed telecommunication between the drone and its controller, avoiding any physical obstacles or signal interference from the surrounding environment. These factors should be evaluated to select an optimal takeoff point, ensuring the safety and effectiveness of the UAV monitoring mission.

Note S4. Environmental conditions of the field campaign and flight mission summary

Table S1: Summary of environmental conditions and conducted flight missions during the field campaign from September to December 2023. The temperature and wind speed values provided are the recorded averages. The atmospheric stability class for each flight mission was estimated using the Pasquill stability classes (Seinfeld and Pandis, 2016).

Date	Start time	End time	Temperature [$^{\circ}C$]	Wind speed [m s^{-1}]	Atmospheric stability	Flight mode
09/09/23	11:56:37	12:19:16	22.0	2.0	A-B	Hovering
	14:01:57	14:24:23	23.4	3.1	B	Hovering
	14:29:37	14:52:02	23.9	2.5	B	Hovering
09/23/23	11:46:49	11:57:14	20.0	3.5	A	Non-hovering
	12:00:40	12:13:34	20.2	3.0	A-B	Non-hovering
	12:17:09	12:32:21	20.4	4.1	A-B	Non-hovering
	14:13:03	14:28:14	21.3	3.8	B	Non-hovering
	14:31:35	14:44:29	21.3	3.7	B	Non-hovering
	15:04:21	15:30:27	21.5	4.5	B	Hovering
	15:59:06	16:21:26	21.4	2.5	B	Hovering
	16:25:11	16:35:37	21.6	2.2	B	Non-hovering
	16:39:07	17:01:17	21.6	2.9	B	Hovering
	17:04:43	17:27:02	21.9	3.5	B	Hovering
11/04/23	10:49:10	11:11:32	17.4	3.1	B	Hovering
	11:36:39	12:02:10	17.5	4.5	B	Hovering
	12:56:42	13:19:44	17.9	4.8	B	Hovering
	14:32:38	14:43:02	18.4	2.7	B	Non-hovering
	14:46:32	15:08:52	18.3	3.1	B	Hovering
	15:30:24	15:40:44	18.6	3.3	B	Non-hovering
	15:43:50	16:06:10	18.9	3.9	B	Hovering
11/18/23	09:18:15	09:28:45	1.1	5.6	B	Non-hovering
	10:02:09	10:24:25	2.4	6.3	A-B	Hovering
	10:50:56	11:01:25	3.0	5.7	A-B	Non-hovering
	11:46:05	12:08:33	4.2	6.2	A-B	Hovering
	13:40:24	15:01:30	5.0	7.2	A-B	Non-hovering
	14:42:00	15:04:15	6.3	8.6	A-B	Hovering
	15:30:34	15:53:02	7.0	7.1	B	Hovering
12/02/23	09:13:05	09:23:30	2.2	3.4	B	Non-hovering
	09:28:58	09:51:19	2.9	2.9	B	Hovering
	10:16:44	10:27:11	3.6	2.6	B	Non-hovering
	10:31:52	10:54:15	3.9	3.0	B	Hovering
	12:41:51	14:04:46	5.5	2.4	A-B	Non-hovering
	13:55:20	14:05:45	7.6	4.6	A-B	Non-hovering
	14:09:05	14:31:28	8.3	5.0	B	Hovering
	15:10:17	15:33:21	8.7	8.4	B	Hovering

Note S5. Autopilot configuration and mission execution

Initially, the UAV was manually operated around the incinerator stack to identify key factors for the autopilot setup (Table S2).

Table S2: Designated factors considered for setting up autopilot route mapping for the boundary flight mission.

Category	Factor	Information	Value
Boundary flight	$D_{s,h}$	Horizontal distance from the stack center	30 m
	Δ_V	Vertical interval between each layer	5 m
	N_{layer}	Number of layers	9 (for non-hovering flight) 3 (for hovering flight)
Hovering flight	D_{hv}	Distance between hovering points	10 m
	t_{hv}	Time spent in each hovering point	10 seconds

Following this preliminary site investigation, flight routes for the autopilot were established using Google Earth Pro. The paths were plotted according to the designated boundaries, with applicable longitude and latitude coordinates for each flight path and hovering point. The resulting path file was exported in the *.kml* format and then imported as a 'waypoint mission' into the DJI controller. Utilizing the 'Pilot 2' application, flight parameters such as speed, altitude for each waypoint, and hovering duration were set. The UAV's flight speed for these field experiments was consistently maintained at $5\,\mathrm{m\,s^{-1}}$. After finalizing the autopilot configuration on the controller, the anticipated flight time was confirmed to be within the targeted range of 20-25 minutes.

In addition, to maximize the efficiency of flight missions within a single day, six pairs of DJI TB60 intelligent flight batteries were used in rotation, being charged at the DJI BS60 intelligent battery station throughout the day. This ample battery supply, combined with the autopilot system, enabled the continuous execution of multiple flight missions each day during the field experiments.

Note S6. Statistical metrics for model-based and observation-based plume centerline analysis

Table S3: Statistical metrics for a comparative analysis between model-based and observation-based estimations of the plume centerline characteristics. y_i represents experimentally determined values for plume characteristics (centerline altitudes and directions) from the CO_2 concentration data, and $\hat{y}_i$ represents the corresponding model calculation values.

Metrics	Abbreviation	Equation
Root mean square error	RMSE	$\sqrt{\frac{1}{n}\sum_{i=1}^{n}(\hat{y}_i - y_i)^2}$
Mean absolute error	MAE	$\frac{1}{n}\sum_{i=1}^{n}\lvert\hat{y}_i - y_i\rvert$

Note S7. Validation of CO_2 sensor performance through comparison with Gaussian plume model predictions

Sensor performance validation was further conducted by comparing peak CO_2 concentrations observed during each flight mission against calculated plume center concentrations derived from the Gaussian plume dispersion model (Briggs, 1984) (Equation 1). This comparison aimed to verify that peak concentrations detected by the sensors align with theoretical maximum CO_2 concentration values predicted by the model. For these calculations, the CO_2 emission rate (Q) was sourced from data provided by the incinerator plant's management, which was calculated based on the IPCC guidelines (IPCC, 2006), quantified as 63,336 tons annually. Wind speed (U) was measured using the UAV's anemometer for each flight, while σ_y and σ_z values were determined using Pasquill-Gifford (PG) coefficients at a distance of 30 m from the stack, as detailed in Seinfeld and Pandis (2016). Given the focus on plume centerline concentration, the crosswind distance (y) is set to zero, and the vertical distance (z) is equal to the effective plume height (H), as estimated by the plume rise model. Concentration units were converted from $\mathrm{kg\,m^{-3}}$ to parts per million utilizing the ideal gas law to facilitate direct comparison. For this conversion, we used the averaged values of ambient temperature and pressure, recorded by the UAV's onboard sensors at one-second intervals, for each flight mission.

$$C(x, y, z) = \frac{Q}{2\pi U \sigma_y \sigma_z} \exp\left(-\frac{y^2}{2\sigma_y^2}\right)\left[\exp\left(-\frac{(z+H)^2}{2\sigma_z^2}\right) + \exp\left(-\frac{(z-H)^2}{2\sigma_z^2}\right)\right] \tag{1}$$

The analysis illustrated by Figure S4 revealed that for hovering flights, the observation-based estimation of the peak CO_2 concentrations closely matched the model-based calculated values, with a mean calculated concentration of 2,429.7 ppm versus a mean observed peak concentration of 2,332.2 ppm. Conversely, a notable variance was observed in non-hovering flight data, where the mean calculated concentration was 2,736.0 ppm, but the mean observed peak concentration was significantly lower at 998.1 ppm. This discrepancy reaffirms the findings presented earlier, indicating the enhanced detection capability of sensors during hovering flights for capturing higher CO_2 concentrations, compared to the more limited efficiency in non-hovering flights.

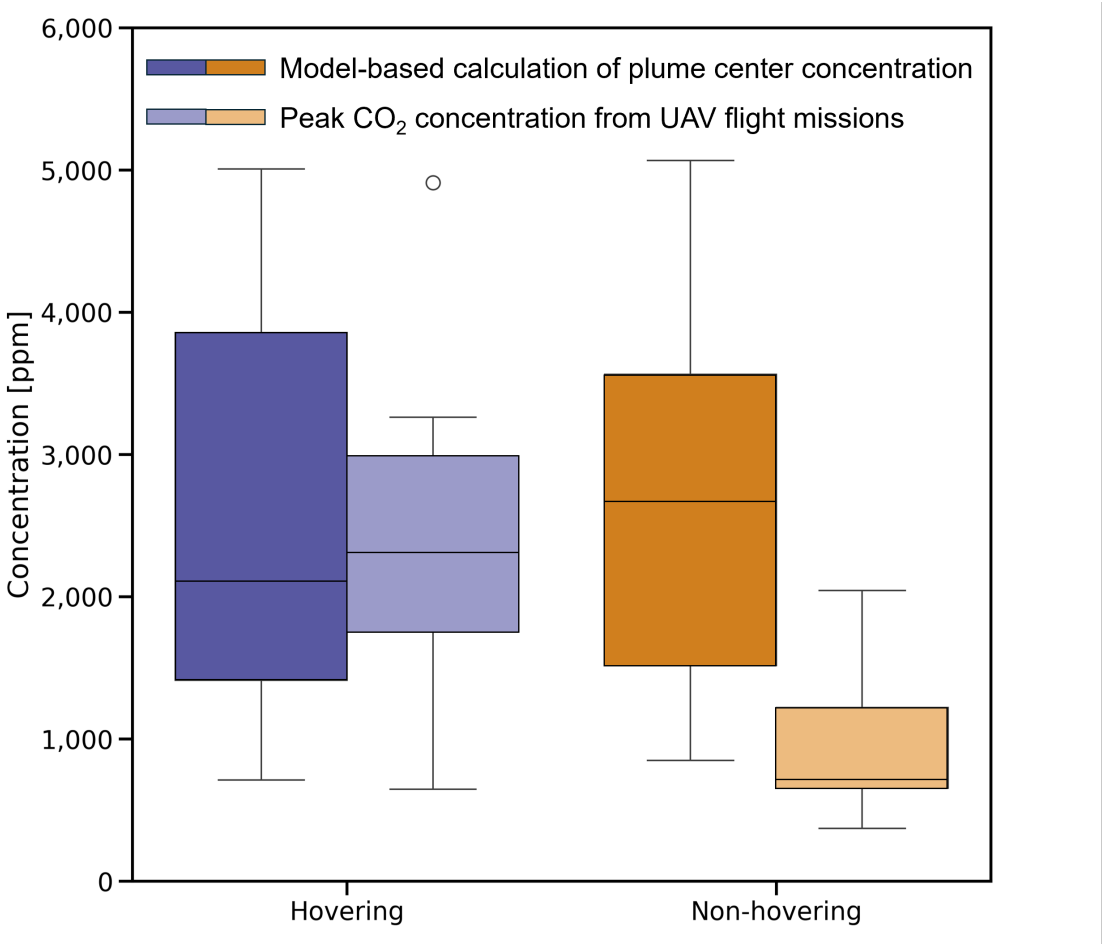

Figure S4: Comparison between calculated plume center concentrations using Equation 1 and observed maximum CO_2 concentrations from flight missions, categorized by hovering status and presented as boxplots.

Note S8. Variability on sensor responses near the peak CO_2 concentration location

Table S4: Information on the sensor response times according to manufacturer specifications and the empirical discrepancies observed between the peak CO_2 concentration timings and peak measurements of other pollutants for each sensor type. The observation was obtained from 15 hovering flight mode missions. Details regarding the manufacturer specifications can be found in the SI Note S2.2

Pollutants	Sensor response time as documented in manufacturer specifications	Temporal discrepancy between the peak CO_2 concentration and the peak levels of other pollutants
CO_2	<3 s (500 ml/min)	-
VOCs	<3 s (diffusion mode)	2 s
PM_{10}	<10 s (overall response time)	1 s
CO	<20 s (t_{90}, 0-10 ppm)	6 s
O_3	<45 s (t_{90}, 0-1 ppm)	6 s
H_2S	<55 s (t_{90}, 0-2 ppm)	11 s
NO_2	<60 s (t_{90}, 0-2 ppm)	6 s

Note S9. Impact of temporal gaps on plume center detection in the hybrid flight strategy

To further validate the effectiveness of the proposed hybrid flight strategy, we also investigated the impact of the temporal gap between non-hovering and subsequent hovering flights on the consistency of plume center detection. Instead of limiting the analysis to directly sequential flights, the scope was broadened to include a range of intervals, from immediate subsequent flights to those with several intervening flights. This examination aimed to understand the potential variability in plume center detection over time, acknowledging that such variations might be influenced by specific site characteristics and prevailing meteorological conditions.

Figure S5 demonstrates that the absolute differences in both plume center altitude and direction tend to widen with increasing temporal gaps between non-hovering and hovering flight modes. This observation suggests a potential threshold for the effective implementation of the hybrid flight strategy, emphasizing the importance of closely timed sequential flights to ensure reliable plume detection and accurate concentration measurements.

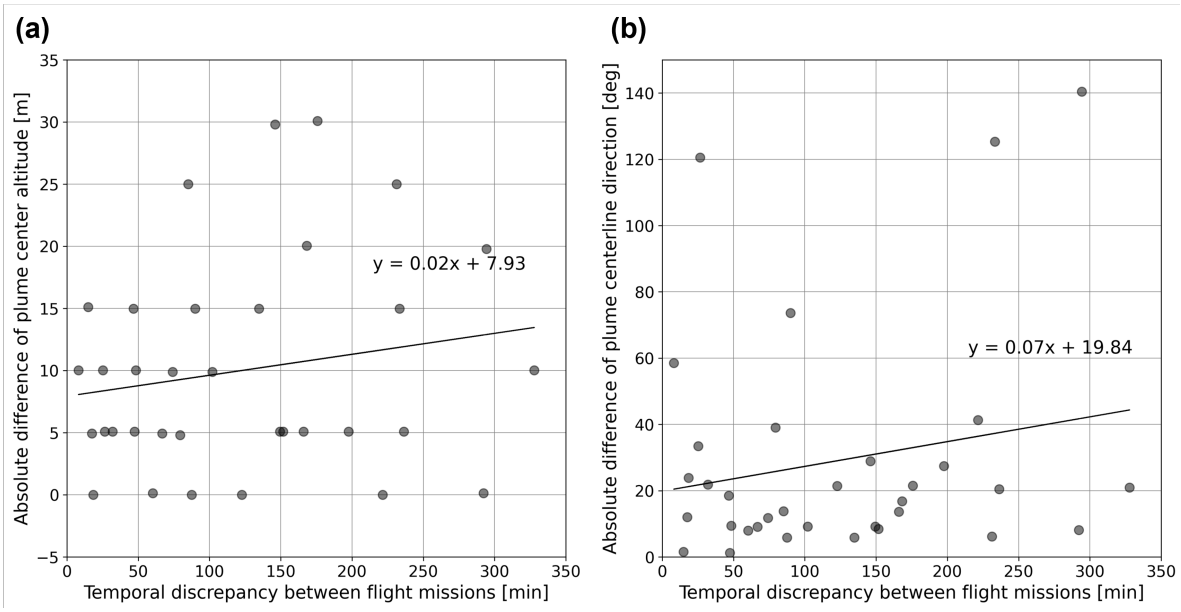

Figure S5: Absolute differences in plume center characteristics with varying temporal intervals between sequential flight missions: (a) displays the variation in plume center altitude, and (b) shows the variation in plume centerline direction.

References

Briggs, G.A., 1984. Plume rise and buoyancy effects, in: Randerson, D. (Ed.), Atmospheric Science and Power Production. U.S. Department of Energy, Springfield, U.S.A., pp. 327–366. DOE/TIC 27601.

IPCC, 2006. 2006 IPCC Guidelines for National Greenhouse Gas Inventories. Institute for Global Environmental Strategies (IGES), Hayama, Japan, Hayama, Kanagawa, Japan. URL: http://www.ipcc-nggip.iges.or.jp. prepared by the National Greenhouse Gas Inventories Programme, Eggleston H.S., Buendia L., Miwa K., Ngara T., and Tanabe K. (eds.).

Seinfeld, J.H., Pandis, S.N., 2016. Atmospheric chemistry and physics: from air pollution to climate change. John Wiley & Sons.